

Classification
Physics Abstracts
07.75 — 07.80

From direct ion images to ion probe scanning

Georges Slodzian ⁽¹⁾, Bernard Daigne ⁽²⁾ and François Girard ⁽²⁾

⁽¹⁾ Laboratoire de Physique des Solides, Bât. 510, Université Paris-Sud, 91405 Orsay Cedex, France

⁽²⁾ O.N.E.R.A., B.P. 72, 92220 Châtillon Cedex, France

(Received June 03, 1992, accepted June 09, 1992)

Résumé. — L'opposition entre "image ionique directe" et "image par balayage avec une sonde" a été reconsidérée du point de vue de la transmission et de la résolution spatiale. Pour cela, l'éclairement dans la tache d'aberration donnée par l'objectif à immersion d'un objet ponctuel (réponse percussive) a été calculé en tenant compte de la distribution énergétique des ions secondaires et de la valeur maximale Φ_{om} de l'énergie latérale fixée par un diaphragme placé au niveau de la pupille. La transmission de l'objectif et sa limite spatiale de résolution ont été évaluées en fonction de Φ_{om} et pour une bande d'énergie donnée. Les résultats sont comparés à ceux obtenus avec une sonde lorsque l'objectif est utilisé simplement comme un système de collecte des ions. Les gains de transmission ont été évalués en tenant compte des limites imposées à l'étendue du faisceau par le pouvoir séparateur en masse du spectromètre.

Abstract. — Direct imaging with secondary ions *versus* scanning with an ion probe have been considered from the transmission and lateral resolution standpoints. Ions emitted from an object point are focused by an immersion lens into an aberration spot. The illumination in the spot (spread function) has been computed, taking into account the energy distribution of secondary ions and the upper limit Φ_{om} the lateral initial energy fixed by a material stop in the plane of the crossover. Transmission and spatial resolving limit have been evaluated *versus* Φ_{om} for a given energy bandwidth. The results are compared to those obtained with an ion probe when the objective lens is working simply as a collecting system. The gains in transmission are evaluated in relation with limitations introduced by the spectrometer according to the mass resolving power being used.

1. Introduction.

It is not a secret that Raimond Castaing, after the successful achievement of his electron microprobe, regretted that no optical system were available for focusing X-rays directly into an image made of one selected characteristic line. As a consequence, compositional maps could be obtained only "artificially" by scanning the probe. The emission of secondary ions induced by the impact of primary ions of a few keV energy gave him the opportunity of both a "revenge" and a beautiful exercise in charged particle optics. Indeed, one knows that electrons emitted from a surface can

be focused directly into an image by means of an immersion objective lens [1]. Dealing with secondary ions, that is with the emission of spontaneously ionized sample atoms, the objective lens will produce a direct ion image which is a superposition of many images each of them being made of a given ionic species. A mass spectrometer (of a special design) should then allow to select specific ion images and to get a set of micrographs, with lateral resolutions of about one micrometer, representing the distribution of the elements and their isotopes composing the sample. This was the basic idea Raimond Castaing proposed to one of us (G.S.) at the end of the fifties and which has been carried out under his supervision in the years which followed [2]. A commercial instrument, derived from this work, has been built by Cameca and has evolved receiving different names, SMI300, IMS3F, IMS4F, ... [5, 6]. To pay tribute to Raimond Castaing for opening, more than thirty years ago, a domain of research and applications which is still developing, this paper will be devoted to the re-examination of the opposition between "direct ion imaging" and "imaging with a scanning ion probe".

Our contribution will be centered about the transmission problem which means that we will try to evaluate the fraction of the emitted signal contributing to the image. This particular aspect has been chosen because the production of secondary ions implies the ejection of atoms from the target and results in the fact that an analysis cannot be started again on the same sample exactly so that any collection deficit may become irreparable. The fundamental parameter controlling the ultimate possibilities of the method is the "useful yield" which can be defined as the inverse of the average number of atoms of a given element which must be ejected to detect one characteristic ion of that element. Obviously, the lesser the collection losses the higher the useful yield. However, one should keep in mind that although efficient collection is necessary it cannot be a substitute for poor ion production yields. In this paper we will leave aside the questions concerning the experimental conditions leading to high ion yields because it would imply a rather lengthy review of the ionization processes.

In the limited field of our subject we will not address a few other relevant questions such as bombarding and vacuum conditions, data recording and processing, acquisition times. Neither will we make a review of the probe instruments from the beginning [7, 8] until the new machines which have appeared after progress made in ion sources [9, 10], in time of flight mass spectrometers [11, 12] and in more efficient optical schemes for collecting and mass analyzing secondary ions with magnetic spectrometers [13].

In this work we have calculated the potential map inside the objective lens and ion trajectories have been integrated by numerical methods. Although calculations have been applied to the optical scheme of the IMS4F, the detailed structure of this instrument is of no importance here since only a few features are involved, namely the objective lens itself and general data about the double focusing magnetic mass spectrometer. The reason for that choice is that we plan to compare calculations with experiments on the instrument in our laboratory. Besides, the study of a concrete case is thought to be a good example to bring out the actual limits and to locate where further progress can be made.

2. Immersion objective lens.

2.1 GENERAL DESCRIPTION. — The schematic diagram of the objective lens is given in figure 1. A plane object M , at a potential V , is followed by three electrodes S_1, P, S_2 with revolving symmetry about a common axis, orthogonal to the surface of M , which defines the optic axis of the objective lens. It will be convenient to consider the action of different parts of the objective lens separately: on the one hand, the section between M and S_1 where the particles experience an accelerating field and, on the other hand, the focusing section composed of the three electrodes

(S_1 , P , S_2) where P is polarized by an adjustable voltage. We will refer to this last section as “lens L ” as if it were a classical three electrode electrostatic lens.

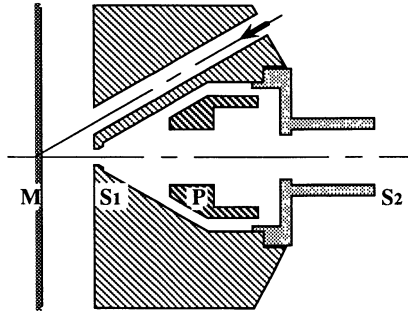


Fig. 1. — Schematic diagram of an immersion objective lens. M , plane sample at acceleration voltage V . S_1 and S_2 grounded electrodes, P , control electrode polarized with an adjustable voltage. The arrow shows the direction of the incoming primary ion beam.

The operation of the objective lens is the following: the accelerating field produces a virtual image of the sample surface with angular and chromatic aberrations⁽¹⁾, and this image is transformed into a real one by the action of the converging section L . At the exit of the objective lens there is an illuminating pupil which is the ideal place where to put a diaphragm for stopping down the aperture of the pencils of ionic trajectories converging in each point of the image. This diaphragm is called a “contrast diaphragm” and since it determines the aperture of the ionic pencils, it controls the amplitude of the aberrations and consequently the lateral resolution in the image. We will recall the main properties of the objective lens and describe them in the framework of trace space diagrams [14].

2.2 OBJECTIVE LENS IN TRACE SPACE.

2.2.1 Trace diagrams — It is quite easy with a computer to draw trajectories stemming from an object point and follow what happens to them as they travel through the objective lens. To simplify the presentation we will only consider meridian trajectories. Particular interest will be given to the ions emitted from the central point of the sample, that is to the point which is at the intersection of M and the optic axis. In this case, the beam of trajectories will have the rotational symmetry about the optic axis.

Let us take a fixed meridian plane and let the cartesian coordinates (x, z) represent the position of a point where z is the abscissa along the optic axis and x the ordinate along an axis orthogonal to the former. At abscissa z , trajectories are characterized by the values of two variables, x and $p = dx/dz$, that is by their transverse displacement from the optic axis, x , and their slope, p . It is convenient to represent a trajectory by a point in a two dimensional space where x and p are respectively its abscissa and its ordinate. A set of trajectories in a transverse cross-section of the beam relative to the optic axis, is represented by a set of points which form a trace diagram. The practical interest of such diagrams is, among others, to transform the inextricable tangle of lines obtained when trajectories are drawn in the ordinary geometric space, into a clear display

⁽¹⁾ By analogy with light optics, “chromatic” refers to differences in focusing due to differences in ion energies.

of data which gives a simple access to the complex structure of a beam composed of particles with different energies. Besides, the calculation of a limited number of trajectories is very often sufficient for bringing out the structure of the beam.

2.2.2 Monokinetic beam. — Let us consider ions emitted from a given point in M with an initial kinetic energy Φ_0 (expressed in electron-volts) and let α_0 be the angle of their velocity with the normal to M, α_0 covers the whole range of values from $-\pi/2$ to $\pi/2$. At the exit of the objective lens, the points representing the trajectories in the trace space are found along a well defined curve $\Gamma(\Phi_0)$ with edges corresponding to emission angles equal to $\pm \pi/2$. It is enough to calculate a ten or so trajectories to draw the shape of the curve Γ and know the structure of the beam at a given abscissa z along the optic axis. When z changes the shape of Γ changes also.

In a drift space, the slope p remains constant so that moving from $z = Z_i$ to z makes the representative point in the trace space move from (X_i, p) to (x, p) , x and X_i being linked by the simple relation $x = p(z - Z_i) + X_i$. If the slopes are small enough for aperture aberrations to be limited to the third order, the beam stemming from the central point will be represented by a Γ curve which is symmetrical with respect to origin and has the following equation,

$$x \simeq p(z - Z_g) + C_s p^3 \quad (1)$$

where Z_g is the position of the Gaussian image point and C_s the spherical aberration coefficient. The two symmetrical edges of Γ are located on parallel straight lines whose ordinates are $\pm pm$ corresponding to ions emitted with $\alpha_0 = \mp \pi/2$. Besides, Γ has an inflexion point at the origin.

In figure 2, Γ curves are shown for two remarkable positions: the Gaussian image position in Z_g where the tangent at the origin coincides with the y -axis and the position of the least confusion circle where the projection of Γ on the x -axis has the smallest possible length. This length corresponds to the minimum size of the spherical aberration spot.

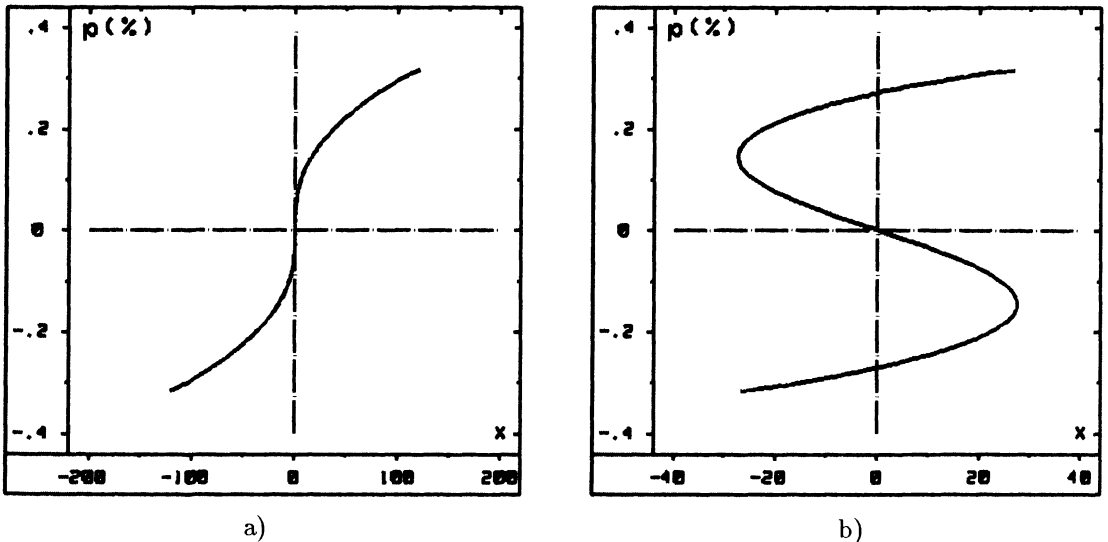


Fig. 2. — Diagrams of a monochromatic beam in the transverse trace space. The $\Gamma(\Phi_0)$ graphs represent ion trajectories with $\Phi_0 = 2$ eV initial energy (p in % and x in μm). Ions are emitted from the central object point with α_0 angles ranging from $-\pi/2$ to $\pi/2$. (a) Gaussian position and (b) least confusion disk position, 180mm and 150mm from the crossover respectively.

2.2.3 Polychromatic beam. — The sputtered ions have a continuous spectrum of initial energies. In general, a limited energy range will be selected by the mass spectrometer. Let Φ_{oi} and Φ_{os} be the lower and upper limits of the energy interval. To get an idea of the structure of the beam it is enough to calculate the Γ curves belonging to the limits Φ_{oi} and Φ_{os} and to a few intermediary energies. As an example, one can look at the diagrams in figures 3a and 3b where the beam has been stopped down as indicated in the next paragraph. The different shapes of the Γ (Φ_0) curves reflect the fact that the objective lens does not focus different energies in the same way ions (chromatic aberration). In a drift space, it is easy to move from one position z to another and follow the changes in the structure of the beam.

2.2.4 Upper limit of the transverse energy. — Near the sample surface the field is nearly uniform so that the velocity component orthogonal to the field direction remains unaltered after a voltage drop U . Thus, after being accelerated by U , ions emitted with Φ_0 and α_0 have a slope nearly equal to $(\Phi_0/U)^{1/2} \sin \alpha_0$ where $\Phi_0 \ll U$. The quantity $\Phi_0 \sin^2 \alpha_0$ is the kinetic energy corresponding to the component of the initial velocity orthogonal to the field direction, it will be referred to as the transverse (or lateral) initial energy. Ions emitted from the sample surface with the same transverse energy form a parallel beam after being accelerated by the voltage drop U . This parallel beam will subsequently be focused into a given point in the second focal plane of the optical system formed by the rest of the objective lens, the distance of this point from the axis is proportional to the slope of the parallel beam, that is, to the square root of the initial transverse energy. As for particles leaving the sample along the normal ($\alpha_0 = 0$), their trajectories will cross the optic axis at the second focal point. If a stop is placed at this "crossover", an upper limit will be imposed upon the transverse energy. This material stop is the "contrast diaphragm" already mentioned and the upper limit of the transverse energy will be referred to as Φ_{om} . Particles with initial energies higher than Φ_{om} will be stopped if their emission angle α_0 is higher than α_{oc} (or lower than $-\alpha_{oc}$) given by the relation,

$$\sin \alpha_{oc} = (\Phi_{om}/\Phi_0)^{1/2} \quad (2)$$

For energies like $\Phi_0 \leq \Phi_{om}$, there is no limitation on the collection.

Let us consider the beam of particles emitted from the central point, each energy $\Phi_0 > \Phi_{om}$ has a Γ (Φ_0) curve symmetrical with respect to the origin with edges corresponding to the emission angles $\pm \alpha_{oc}$ as defined by (2). If $z = Z_c$ refers to the crossover position, all edges of Γ curves corresponding to α_{oc} have the same projection H on the x -axis and those relative to $-\alpha_{oc}$, the projection in H' (Fig. 3a), H and H' being symmetric with respect to origin. The diagram in figure 3a in relative to $\Phi_{om} = 2\text{eV}$, for higher values of Φ_{om} the description given above might be approximate because the aperture aberrations will become more important. With the operating conditions in figure 3a ($\Phi_{oi} = 0$, $\Phi_{os} = 20\text{ eV}$ and $V = 4.5\text{ kV}$), it could be checked that, at $\Phi_{om} = 5\text{ eV}$, aberrations effects amount to a few percents only. Besides, the diagram attached to the beam stemming from an object point in the vicinity of the central point is simply deduced from the former diagram by translation along the y -axis, the edges of the Γ curves having still their projection at H and H' , provided of course the distance between the object point and the central point is small enough to keep field aberrations negligible.

Another remarkable position can be found along the optic axis for $z = Z_a$ as shown in figure 3b. The diagram plotted in this figure represents the beam emitted from the central point when the whole beam is stopped down to $\Phi_{om} = 2\text{ eV}$ by the contrast diaphragm, the limits of the energy band being $\Phi_{oi} = 0$ and $\Phi_{os} = 20\text{ eV}$. The position Z_a is determined by the following occurrence: the straight lines orthogonal to the x -axis and passing through the edges of the $\Gamma(\Phi_{om})$ curve intersect the x -axis at G and G' . They define a portion of trace space inside which the $\Gamma(\Phi_{os})$ curve must fit exactly. In the case of figure 3b, the $\Gamma(\Phi_{os})$ curve is tangent to the vertical lines

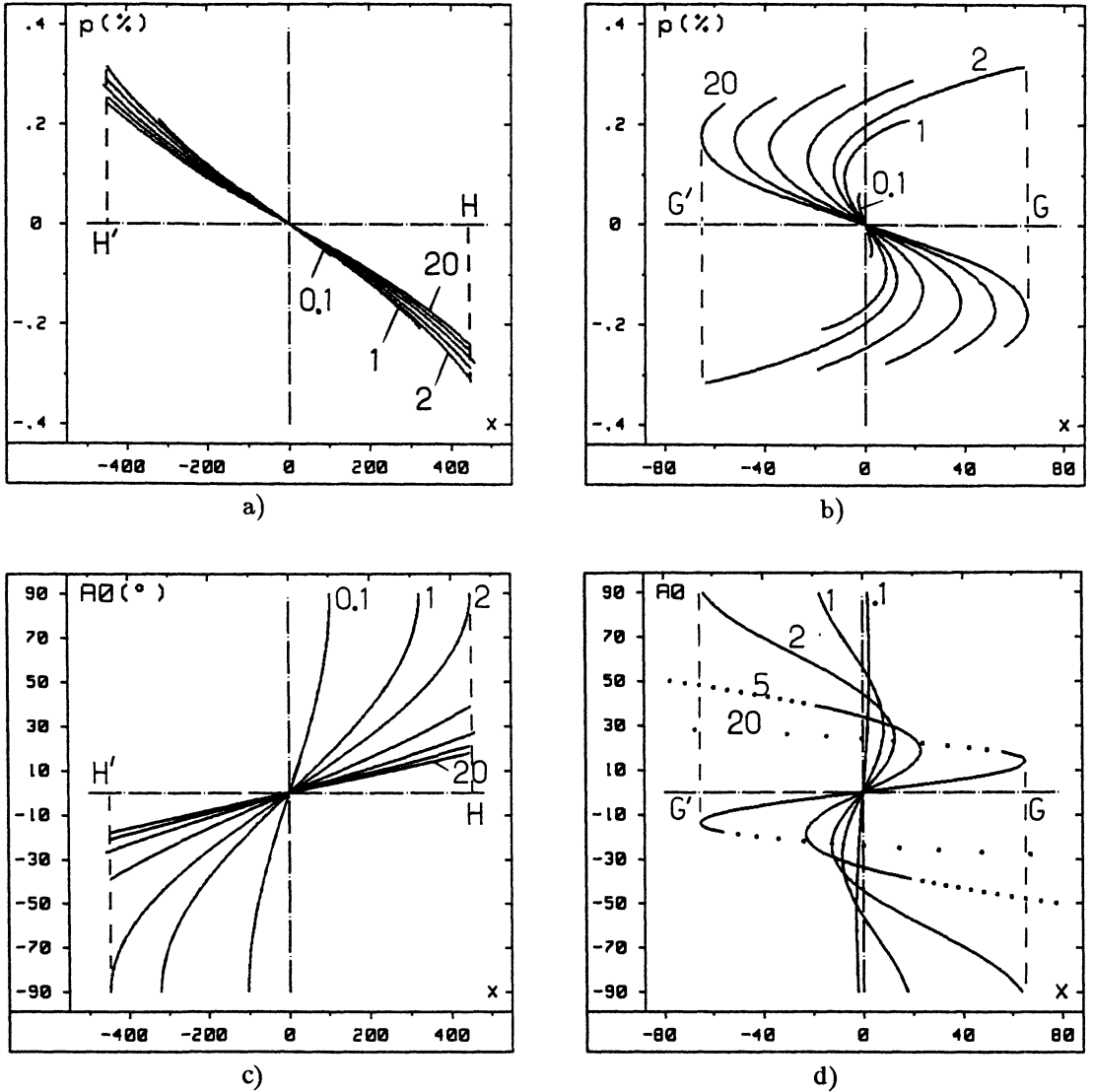


Fig. 3. — Set of $\Gamma(\Phi_0)$ curves representing the action of the objective lens upon a polychromatic beam, the upper limit of the lateral energy being fixed at $\Phi_{0m} = 2$ eV by the diaphragm at the crossover. Slopes p are expressed in % and x in μm . The energies drawn are 0.1, 1, 2, 5, 10, 15 and 20 eV. Trace diagrams (a) in the crossover plane (b) in the image plane (least confusion disk for the whole beam). (c) and (d) diagrams are deduced from (a) and (b) respectively by replacing the slope p with the corresponding $\alpha_0(A_0$ in degrees). In (d) 10 and 15 eV have been suppressed for clarity. The dots stand for trajectories eliminated by the diaphragm at the crossover.

defined above but if a smaller value of Φ_{0m} had been chosen, the aperture aberrations would have been smaller and, instead of being tangent to the vertical lines, the $\Gamma(\Phi_{0s})$ curve would have had its edges lying on those lines. The situation described in figure 3b, corresponds to a minimum in the beam diameter and defines the "least confusion disk" for the whole beam. Z_a can also be considered as defining the position of the aberrated image of the central point. The diameter D_a

of the aberration disk and its position Z_a depend upon Φ_{om} , Φ_{oi} and Φ_{os} . From now on we will take $\Phi_{oi} = 0$.

It should be noted, specially after a beam transport operation, that the minimum of the beam diameter may not occur at the position Z_a we have just defined. Instead, the waist of the beam⁽²⁾ may occur at the crossover position. Nonetheless, the previous definition of the position of the aberrated image of the central point is still valid because it can be easily worked out that Z_a corresponds to the best separation between the aberration disks associated with two neighbouring object points.

The diagrams in the figures 3c and 3d have been deduced from those in the figures 3a and 3b respectively by replacing each slope p by its associated α_0 emission angle. In figure 3c, it can be easily seen how the upper limit of the emission angles is progressively reduced as the initial energy increases from Φ_{om} to Φ_{os} . In this respect, it is interesting to observe that if a diaphragm had been placed in the plane of the least confusion disk (Fig. 3d), angular discriminations would be much more complicated to figure out because of the shape of Γ curves due to aperture aberrations. The comparison with the former case shows that the simplest situation results from a beam being stopped down at the crossover position.

Once the energy bandwidth has been fixed at $(0, \Phi_{os})$, the position Z_a and the diameter D_a of the least confusion disk varies with Φ_{om} as shown in tables II and III. D_{ao} is the diameter of the aberration spot once referred back to magnification unity. In a first approach, it gives an idea of what one may expect for the lateral resolving limit. However, ion micrographs seem to have a much better lateral resolution than the values of D_{ao} would suggest. The reason is that until now only the geometry of the beam has been described and this description does not account for the distribution of intensity inside the diameter D_a of the aberration spot.

3. Illumination in the aberration spot.

3.1 GENERAL CONSIDERATIONS. — It is classical to characterize optical systems by determining the "spread function". In our case, it will take the form of a function $f(r)$ giving, in a transverse cross-section of the beam relative to the optic axis at position z , the number of particles arriving per unit time and unit area around a point located at a distance r from the optic axis when the object emission is defined by the number of particles emitted, per unit time and unit area, from a infinitesimal area around the sample central point.

The function $f(r)$ will depend upon the energy distribution of the ionic species being considered. Distributions recorded for C^- and C_2^- ions emitted from a vitreous carbon sample bombarded with Cs^+ ions of 14.5 keV energy, have been used. The data shown in figure 4 have been corrected for angular collection discrimination and are normalized which means that we have plotted the derivative $dn/d\Phi_0$ where $n(\Phi_0)$ is the ratio $N(\Phi_0)/N_T$ of the number $N(\Phi_0)$ of ions of given species emitted between 0 and Φ_0 to the total number N_T of ions of that species.

To make the calculations the simplest possible, we will assume that the angular distributions of the emitted ions have the revolving symmetry about the normal and that they follow a cosine law ($\cos \alpha_0$) for all energies. Then, for an fixed energy bandwidth of $(0, \Phi_{os})$, the intensity $I(\Phi_{om})$ emitted per unit area around an object point is calculated as a function of the upper limit Φ_{om} of the lateral energy. Now, if I_T refers to the total intensity emitted per unit area around an object point, the transmission $T(\Phi_{om})$ can be defined as the ratio $I(\Phi_{om})/I_T$. In figure 5, $T(\Phi_{om})$ has been plotted *versus* Φ_{om} for C^- and C_2^- ions when Φ_{os} is fixed at 20 eV. It is worth noting that the cosine law leads to a filtering coefficient equal to Φ_{om}/Φ_0 .

⁽²⁾ The waist of the beam refers to the minimum diameter of the beam envelope.

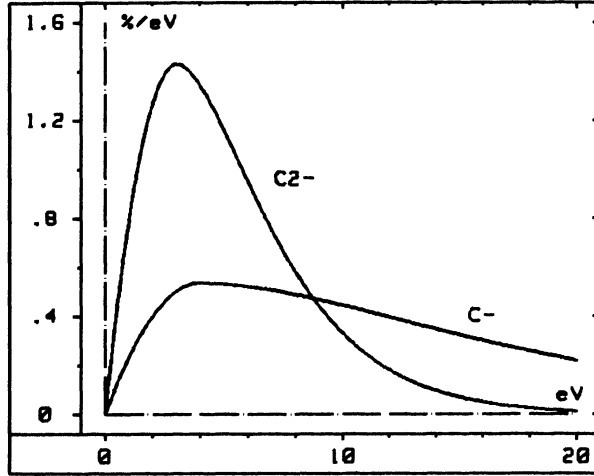


Fig. 4. — Energy distribution curves of C^- and C_2^- secondary ions emitted from a vitreous carbon sample bombarded with Cs^+ ions of 14.5 keV energy. The X -axis is graduated in electronvolts, the Y -axis represents the derivative $dn/d\Phi_0$ where n is the ratio $N(\Phi_0)/N_T$ of the number of ions emitted between 0 and Φ_0 to the total number of emitted ions of a given species.

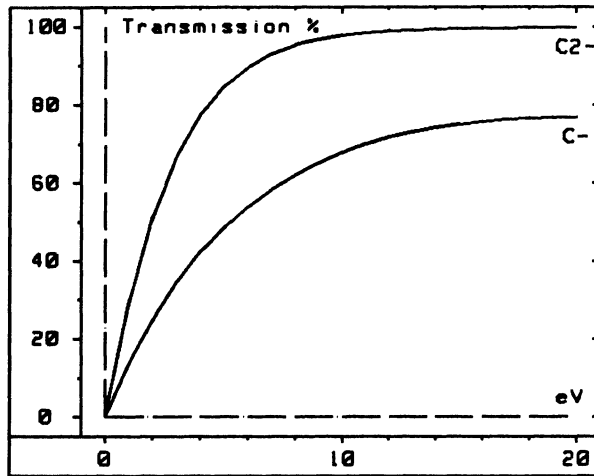


Fig. 5. — Transmission $T(\Phi_{om})$ versus the cutoff Φ_{om} of lateral energy for [0.20] energy bandwidth and two ionic species C^- and C_2^- . The X -axis is graduated in electronvolts.

Let us consider the beam stemming from an infinitesimal area dS_0 around the sample central point, this beam will have a rotational symmetry about the optic axis. Then let us define $I(r; \Phi_{om})$ by the relation $dF(r; \Phi_{om}) = I(r; \Phi_{om})dS_0$ where dF is the intensity inside the circle of radius r in a cross-section of the beam after the objective lens when the upper limit of the lateral energy has been set at Φ_{om} . By definition of $f(r)$ and $I(r; \Phi_{om})$ we have,

$$I(r; \Phi_{om}) = \int_0^{D_i/2} 2\pi r f(r) dr \tag{3}$$

where D_i is the diameter of the circle, $D_i = 2r$. For a cross-section in the image plane, $z = Z_a$, if D_i is greater than or equal to the diameter D_a of the least confusion disk, the integral in (3) will be equal to $I(\Phi_{om})$. Actually, the interesting point is to determine how the intensity $I(\Phi_{om})$ is distributed then, it is more convenient to introduce the normalized functions like,

$$J(r; \Phi_{om}) = I(r; \Phi_{om})/I(\Phi_{om}) \text{ and } \varphi(r) = f(r)/I(\Phi_{om}). \tag{4}$$

A relation similar to (3) can be written down where $f(r)$ would be replaced by $\varphi(r)$ and $I(r; \Phi_{om})$ by $J(r; \Phi_{om})$. With D_i equal to D_a we have $J(r; \Phi_{om}) = 1$ and the same occurs for the integral. Let us also mention that $dJ/dr = 2\pi r \varphi(r)$.

Let us consider an extended sample area around the central point and let us assume that the shape of the spread function $f(r)$ remains about the same as long as the object points are not too far from the optic axis⁽³⁾. Then, let B_0 be an object point and B_1 its geometrical image which coincides with the center of the aberration spot in the cross-section being considered. The position of B_1 is defined by its cartesian coordinates (z_1, y_1) in the transverse plane of the cross-section, the coordinates (x, y) referring to an ordinary point Q. The spread function associated with B_1 is obtained by replacing r in the previous $f(r)$ function by ρ where $\rho^2 = (x - x_1)^2 + (y - y_1)^2$. Thus at any geometric image point with coordinates (x_1, y_1) is associated a spread function $f(\rho) = f(x - x_1, y - y_1)$. If the illumination of the geometric image, number of particles per unit time and unit area in the transverse plane being considered, is given by the function $Ob(x_1, y_1)$, the illumination $E(x, y)$ around Q is given by,

$$E(x, y) = \int \int Ob(x_1, y_1) f(x - x_1, y - y_1) dx_1 dy_1 \tag{5}$$

The Fourier transform of $f(r)$ is the transfer function currently used in optics to compare instrument for performances. We will not go into image reconstruction problems using the transfer function, we will only use equation (5) to calculate $E(x, y)$ for given test samples.

3.2 UNIFORM ACCELERATING FIELD. — In the objective lens under consideration here, the accelerating field is practically uniform over most of the space between M and S_1 , it is therefore interesting to study the optical properties of an uniform field first and then to use the results for reference. In other words, let us imagine that the surface of electrode S_1 facing the sample is flat and parallel to M and that there is no hole in S_1 . The electrical field is then V/ℓ where ℓ is the distance between M and S_1 .

3.2.1 Aberrations. — An ion starting from the sample follows a parabolic trajectory which will intersect S_1 and from there on, its trajectory can be characterized by the couple of variables, position and slope at the intersection point, as if this trajectory were a straight line in an ordinary drift space. Of course, those prolonged trajectories are virtual. Approximate analytical calculations allow to determine the focusing properties which can be summarized as follows:

- Ions with energy Φ_0 have prolonged trajectories which lean on a virtual caustic curve similar to that of a spherical aberration. Rays corresponding to emission angles $\alpha_0 = \pm 90^\circ$ seem to stem

⁽³⁾ This assumption means that we may neglect field aberrations such as field curvature or chromatic magnification aberration.

from a point at a distance ℓ behind the sample surface where it is convenient to place the origin of the abscissa. The least confusion disk has its position given by

$$Z_a \simeq 0.70(\Phi_0/V)^{1/2}\ell \tag{6}$$

and its diameter is

$$D_a \simeq 1.2(\Phi_0/V)\ell \tag{7}$$

• If the upper limit of the transverse energy is set at Φ_{0m} and the energy bandwidth defined by $(0, \Phi_{0m})$, the position of the least confusion disk for a polychromatic beam, as long as $\Phi_{0s} \geq 3\Phi_{0m}$, will be given by,

$$Z_a \simeq [(\Phi_{0s} - \Phi_{0m})/V]^{1/2}\ell \tag{8}$$

and its diameter D_a by the expression,

$$D_a \simeq 2\ell(\Phi_{0s} - \Phi_{0m})^{1/2}(\Phi_{0m})^{1/2}/V \tag{9}$$

- The symmetry of the system involves that the magnification of the virtual image is equal to unity.
- The illuminating pupil is at infinity.

One should also note that the diameter of the aberration spot is inversely proportional to the electric field V/ℓ in any circumstances.

3.2.2 Illumination. — To get a first idea of the intensity distribution in a given cross-section of the virtual beam, it is interesting to determine the diameter D_i of the circle containing a fraction h of the intensity $I(\Phi_{0m})$ per unit sample area stemming from an object point, in other words

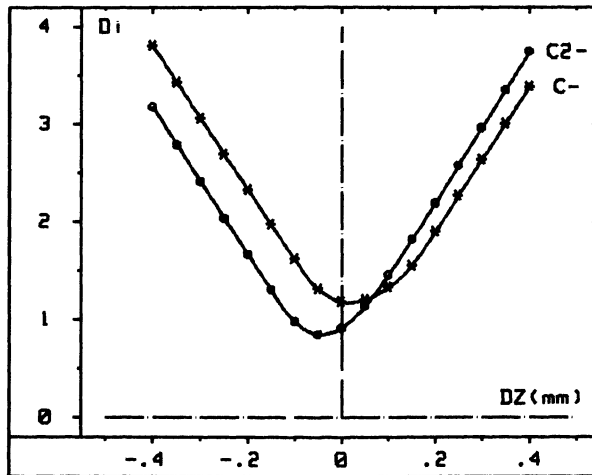
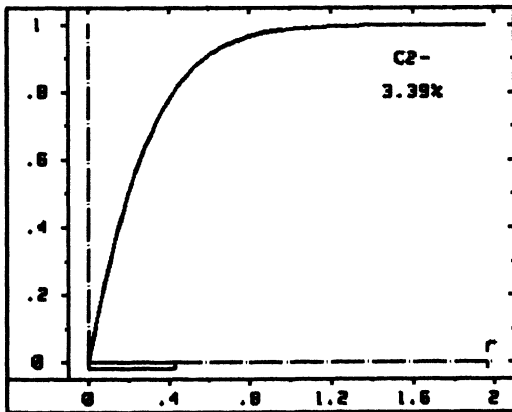


Fig. 6. — Action of an uniform accelerating field upon the ion beam emitted from an object point. Diameter $D_i(\mu m)$ of the disk containing 80% of the intensity $I(\Phi_{0m})$ of the beam stopped down to $\Phi_{0m} = 0.1$ eV and with energies ranging from 0.1 to 20 eV, versus the position D_Z (mm) of the observation plane for C^- and C_2^- ions.

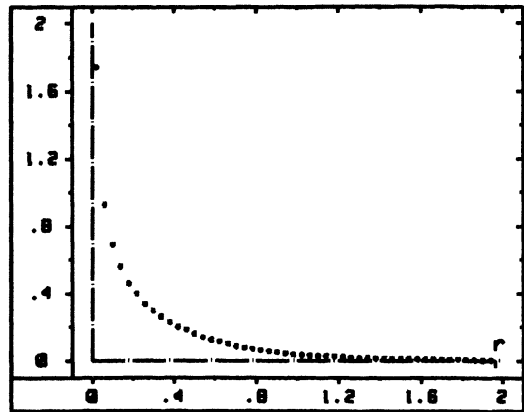
Table I. — Uniform accelerating field. Φ_{om} : upper limit of the lateral initial energy. D_a , diameter and Z_a , position of the image aberration spot from an object point (Z_a being measured from an origin at a distance ℓ behind the emitting surface). ΔZ_a position difference, with reference to the image spot, of the disk having the smallest diameter D_{im} containing 80% of the intensity of the beam stopped down to Φ_{om} . T : transmission after stopping down to Φ_{om} .

$\ell = 4.7 \text{ mm}$ $V = - 4.5 \text{ kV}$			C^-			C_2^-		
Φ_{om} (eV)	Z_a (μm)	D_a (μm)	ΔZ_a (μm)	D_{im} (μm)	T (%)	ΔZ_a (μm)	D_{im} (μm)	T (%)
0.1	310	2.8	- 90	1.2	1.5	- 170	0.8	3.4
1	305	8.8	- 85	3.6	14	- 165	2.6	30
2	300	12	- 77	5.0	25	- 160	3.5	51
5	270	17.5	- 51	7.4	49	- 130	4.8	85

we will solve for r the equation $J(r; \Phi_{om}) = h$. In figure 6, the graphs of D_i versus the positions of the transverse cross-section plane have been plotted for C^- and C_2^- . Those graphs result from calculations made with $\Phi_{om} = 0.1 \text{ eV}$, $\Phi_{os} = 20 \text{ eV}$ and $h = 80\%$. It can be seen that D_i goes through a minimum, D_{im} and Z_{im} will respectively refer to the minimum of D_i and the position along the optic axis where it occurs. In table I, the calculation results for $Z_a, D_a, \Delta Z_a = (Z_{im} - Z_a)$ and D_{im} have been reported as a function of Φ_{om} . It is worth noting that 80% of the intensity stemming from a sample point is found inside a circle whose diameter is much smaller than that of the least confusion disk. This effect is increased for C_2^- ions that is for the energy distribution which has the more pronounced maximum.



a)



b)

Fig. 7. — Illumination in the aberration disk given by an uniform accelerating field. The conditions are those described in figure 6 ($\Phi_{om} = 0.1 \text{ eV}$) and the observation plane at the minimum of the D_i graph for C_2^- ions. (a) Graph of the normalized intensity $J(r)$, r in μm . (b) Graph of $[\varphi(r)]^{1/2}$, r in μm and $\varphi(r)$ in relative transmission per area unit (mm^2) in the observation plane.

In figure 7a the graph of $J(r; \Phi_{om})$ is plotted *versus* r , the calculations being made with $\Phi_{om} = 0.1$ eV, $\Phi_{os} = 20$ eV and for C_2^- ions at a transverse plane position corresponding to the minimum D_{im} (Fig. 6). In figure 7b, the graph of $[\varphi(r)]^{1/2}$ has been calculated with the same conditions as those in figure 7a. The square root has been taken to make more visible the variations of $\varphi(r)$ up to the edge of the aberration spot. However, the determination of $\varphi(r)$ with numerical methods deserves a few comments.

To carry out the calculations with a computer the radius of the aberration spot has to be sliced in small intervals δr (in Fig. 7b, $\delta r = 0.04 \mu m$). First, the difference $\Delta J(r_i; \Phi_{om})$ of the normalized intensities arriving between two successive circles with radius r_i and $r_{i+1} = r_i + \delta r$ has to be determined and the illumination is then deduced by dividing $\Delta J(r_i; \Phi_{om})$ by the area $\pi(r_{i+1}^2 - r_i^2)$. Thus, on each interval δr one gets an average value of $\varphi(r)$. Now, an analytical evaluation of $\varphi(r)$ in the vicinity of the optic axis shows that $\varphi(r)$ is of the order of $1/r$, as a consequence the determination of $\varphi(r)$ may become very sensitive in this region. Particularly, on the optic axis itself, the intensity ΔJ inside the cercle of radius δr is divided by $\pi(\delta r)^2$ so that the result of the calculation is strongly dependant upon the choice made for δr . Although the values obtained for $\varphi(r)$ must be taken with caution in the vicinity of the optic axis, the illumination calculations can be made quite accurately provided the same intervals are used in the numerical integration of expression (5).

3.3 COMPLETE OBJECTIVE LENS. — It can be shown that the perturbation created by the presence of a hole in S_1 is equivalent, in a first order approximation, to a divergent thin lens, with a focal length equal to -4ℓ , located in the plane of S_1 . Strickly speaking, the previous statement is made assuming that electrode P is not polarized but it remains accurate enough for an overall understanding of the objective lens operation even if P is polarized provided S_1 is thick enough. Let us consider the central point A_c , the divergent lens will produce a virtual image A_0 and the crossover, instead of being at infinity, will now be located at the focal point C_0 of the divergent lens that is approximatively at -4ℓ behind S_1 . The convergent section L of the objective lens will produce real images A and C from the virtual objects A_0 and C_0 .

The voltage applied to electrode P can be either of the same sign as that of the particles or of an opposite sign. In the first case the lens L is said to work in the retarding mode and in the second case it works in the accelerating mode. The voltages (Tabs. II and III) have been calculated so as to focus the least confusion disk of the polychromatic beam, defined by $\Phi_{om} = 0.1$ eV and $\Phi_{os} = 20$ eV, at the same distance from the crossover (190 mm) in each mode.

3.3.1 Aberrations. — Calculation results concerning the retarding and accelerating modes are gathered in tables II and III. In the left columns, one can find the data concerning the "geometrical" quantities that is, the position Z_a of the least confusion disk, its diameter D_a as a function of Φ_{om} and D_{a0} which is the diameter D_a expressed at unity magnification. D_{a0} can be compared directly with D_a in table I.

In the particular case of the objective lens being studied here, in which the accelerating and focusing sections can be considered separately to a first approximation, it is instructive to compare the geometrical parameters from tables II and III with those from table I. It can be seen that the effect of the lens L is to increase the diameter of the least confusion disk and that the magnitude of this effect is stronger in the retarding than in the accelerating mode. One can get an overall understanding of those effects by taking into account the chromatic and sperical aberration coefficients for the couple of points (A_0, A) which are the conjugated points previously defined as resulting from the action of L. A more detailed examination has been made and it has shown that when $\Phi_{om} = 0.1$ eV, the degradation comes essentially from the chromatic aberrations, the chromatic aberration coefficient being 3.5 times higher in the retarding mode. Of course, as Φ_{om}

Table II and III. — *Complete immersion objective lens in retarding and accelerating modes. D_a , diameter and Z_a , position of the image aberration spot from an object point (Z_a being measured from the crossover of the objective). D_{a0} : diameter referred back to unity magnification. ΔZ_a position difference, with reference to the image spot, of the disk having the smallest diameter D_{im} containing 80% of the intensity of the beam stopped down to Φ_{om} . D_{im0} : diameter referred back to unity magnification.*

Table II

V = - 4.5 kV V _p = - 3.257 kV				C ⁻			C ₂ ⁻		
Φ_{om} (eV)	Z _a (mm)	D _a (μ m)	D _{a0} (μ m)	ΔZ_a (mm)	D _{im} (μ m)	D _{im0} (μ m)	ΔZ_a (mm)	D _{im} (μ m)	D _{im0} (μ m)
0.1	190	50	5.9	- 16	17.5	2.25	- 24	11	1.5
1	168	140	18.6	- 6	58	8	- 12	37	5.3
2	150	192	28.6	0	87	13	- 4	61	9.3
5	114.5	330	64	11	165	29	11	128	23

Table III

V = - 4.5 kV V _p = 10.8 kV				C ⁻			C ₂ ⁻		
Φ_{om} (eV)	Z _a (mm)	D _a (μ m)	D _{a0} (μ m)	ΔZ_a (mm)	D _{im} (μ m)	D _{im0} (μ m)	ΔZ_a (mm)	D _{im} (μ m)	D _{im0} (μ m)
0.1	190	30	3.6	- 7	12	1.4	- 11	8	1
1	175	90	11.5	0	39	5	- 4	27	3.5
2	162	130	18	+ 5	60	8	1	45	6.2
5	133	248	41.5	+ 11	126	19	11	100	15.2

is increased, the aperture of the ion beam is also increased and the spherical aberrations come into play [16]. It is worth noting that the spherical aberration coefficient is 1.5 times higher in the retarding mode.

α) Remarks upon the spherical aberration.— To evaluate the influence of spherical aberrations of L let us consider a monokinetic beam. As an example let us take $\Phi_0 = 1$ eV with a contrast diaphragm setting Φ_{om} at 1 eV. Calculations for the complete objective lens working in the accelerating mode give about 3.1 μ m for the diameter of the least confusion disk once referred back to unity magnification. This value is much higher than 1.25 μ m given by the accelerating section alone (as calculated from formula (6)). Taking the spherical coefficient due to the action of L alone in the conjugation of the pair A₀ and A and taking the maximum aperture angle after the action of the divergent lens (which can be calculated directly by numerical integration), the evaluation of the spherical aberration diameter gives about 1.8 μ m. Thus, the aperture aberration amplitudes reported here for L and the uniform field are consistent with the aberration diameter calculated directly for the complete objective lens.

It is interesting to note that the spherical aberration due to L alone varies as $(\Phi_{om}/V)^{3/2}$ whereas that due to the uniform field varies as Φ_{om}/V . Thus, the ratio between the two contributions is $(\Phi_{om}/V)^{1/2}$. As a consequence, an increase of the accelerating voltage V will reduce

the contribution of L. For instance, if the voltage V were doubled, the aberrations previously calculated for L and for the uniform field would have had about the same amplitude. It is also worth to mention that in such conditions, with $\Phi_{om} = 0.1$ eV, the aberration due to L would be half that due to the uniform field.

β) Remark about higher accelerating voltage.— Higher accelerating voltages would also be beneficial for reducing the chromatic aberration of L. Indeed, this aberration is proportional to (Φ_{os}/V) $(\Phi_{om}/V)^{1/2}$ whereas the aberration deduced from formula (9) for the uniform field, with Φ_{os} much greater than Φ_{om} , is proportionnal to $(\Phi_{os}/V)^{1/2}(\Phi_{om}/V)^{1/2}$. Thus, the ratio between those two aberration amplitudes varies as $(\Phi_{os}/V)^{1/2}$ which shows that it is possible to reduce the influence of L by increasing V . As an example, calculation results are gathered in table IV for an accelerating voltage which has been doubled with respect to table III.

Table IV. — *Objective lens after doubling the extraction voltage in the accelerating mode.*

V = - 9 kV V _p = 21.154				C ⁻			C ₂ ⁻		
ϕ_{om} (eV)	Z _a (mm)	D _a (μ m)	D _{ao} (μ m)	ΔZ_a (mm)	D _{im} (μ m)	D _{imo} (μ m)	ΔZ (mm)	D _{im} (μ m)	D _{imo} (μ m)
0.1	190	14.4	1.7	- 4	5.6	0.7	- 7	3.9	0.5
1	182	44	5.4	0	19	2.3	- 4	12.7	1.6
2	174	60	7.7	+ 2.5	28	3.5	0	20	2.6
5	114	16.3	41.5	+ 9	54	7.3	+ 7	42	5.75

It should be mentioned that other directions can be explored such as changes in the electrode shapes or the reduction of the size of the objective lens. Geometrical changes are rather difficult to envision in the actual objective lens because of the constraints of the oblique introduction of the beam. With normal incidence better objective lenses could be designed [13].

3.3.2 Illumination. — The two columns labelled C⁻ and C₂⁻ in tables II and III concern illumination calculations in the cross-section of the beam for the two energy distributions given in figure 4. The diameter of the cercle containing 80% of $I(\Phi_{om})$ goes through a minimum D_{im} which occurs at the position given by $\Delta Z_a = (Z_{im} - Z_a)$. D_{imo} is the value of D_{im} at magnification unity. D_{im} , D_{imo} and ΔZ_a have been reported *versus* Φ_{om} . It can be observed that the intensity of beam stemming from the central point is more concentrated near the optic axis than the diameter of the least confusion disk would let guess: roughly speaking, 80% of the intensity is enclosed in a circle with a diameter which is about the third of D_a . This concentration can be understood on qualitative bases.

Let us take the beam stemming from the central point and its cross-section in a transverse plane at abscissa z . The contribution of a given energy to the illumination of a small area surrounding the optic axis, depends upon how well this energy is focused and upon its place inside the energy distribution itself. Roughly speaking, maximal contributions will be achieved at the position z where are focused those energies which are near to the maximum of the distribution⁽⁴⁾. Thus the

⁽⁴⁾ The energy distribution here has to be considered after filtering by the contrast diaphragm.

concentration of the beam will be more emphasized for distributions which have a well marked maximum. As for energies with large deviations from the maximum, they will have a reduced contribution since, on the one hand, they are defocused because of the chromatic aberration and, on the other hand, their supply to the intensity of the beam is intrinsically low because of their position in the actual distribution. As a consequence, the diameter D_{im} and its position Z_{im} depend both upon the shape of the energy distribution and upon Φ_{om} .

The least confusion disk also has a diameter and a position depending upon Φ_{om} and chromatic aberrations but its size is determined by extreme rays of Φ_{om} and Φ_{os} , in conditions where all other energies need only be confined within the aberration spot area.

4. Illumination and spatial resolution for the complete objective lens.

The interesting point in determining $\varphi(r)$ is that it enables us to calculate the illumination of the image of a given sample structure. Let us take, as it is usual in optics, a test sample composed of parallel straight bars laid on a flat substrat. The bars have a periodic spacing $\lambda = 2b$, b being their width. In addition, let E_o refer to the intensity emitted per bar unit area for a given ionic species and let the same parameter relative to the substrat be equal to zero.

Let us consider the geometrical projection of this test sample as if the beam stemming from each object point were composed of particles leaving with a velocity normal to the surface⁽⁵⁾. In a transverse plane chosen as the image plane (2.2.4), the test sample appears at magnification K . If there were no aberrations, the cross-section of the illumination in the direction perpendicular to the bars would be a "square" wave of crenels with period $K\lambda$ and $E_i = E_o/K^2$ height. This ideal pattern is altered by aberrations. For $D_a \leq Kb = K\lambda/2$, the former crenels appear with a flat top and rounded off corners as in figure 8. In this figure normalized values are used which means that the function plotted along the y -axis represents the actual illumination divided by E_i and that on the x -axis, taken along the direction orthogonal to the bars, the unit distance is the width Kb of the geometrical image of a bar. Then, as b is made to decrease, the illumination exhibit a symmetrical modulation about a mean value $\langle E \rangle = E_i/2$. If E_{max} and E_{min} are the illumination maximum and minimum respectively, $E_{max} \leq E_i$ and $E_{min} \geq 0$, it may be convenient to characterize this modulation by a coefficient θ defined by the relation,

$$\theta = (E_{max} - \langle E \rangle) / \langle E \rangle = (\langle E \rangle - E_{min}) / \langle E \rangle \quad (10)$$

For $D_a \simeq Kb$, it comes $E_{max} \simeq E_i$, $E_{min} \simeq 0$ and $\theta = 1$. It may be also worth to calculate the ratio $\eta = E_{min}/E_{max}$ which is equal to $(1 - \theta)/(1 + \theta)$.

Let us look now at a few results obtained with the objective lens working in the accelerating mode and with a beam stopped down to $\Phi_{om} = 0.1$ eV. In the image plane Z_a , both C^- and C_2^- ions have a diameter D_{im} of about $13.2 \mu m$, that is, $D_{imo} \simeq 1.55 \mu m$ at magnification one ($K \simeq 8.5$). If one looks for the modulation obtained with a spacing $\lambda \simeq 3.1 \mu m$, one finds $\theta \simeq 0.82$ and $\eta = 0.1$. The structure of parallel bars can be considered as well resolved⁽⁶⁾.

Similar calculations show that with a spacing $\lambda \simeq 1 \mu m$, $\theta \simeq 0.25$ is obtained or equivalently $(E_{max}/E_{min}) \simeq 1.7$. Thus, although $D_{imo} \simeq 1.55 \mu m$ is larger than the width of a bar ($b \simeq 0.5 \mu m$) and the spacing $\lambda = 1 \mu m$, we can consider that the bar structure is resolved. If we notice that even

⁽⁵⁾ It is implicitly assumed that the object points are near to the optic axis so as to avoid distortion or chromatic magnification aberrations.

⁽⁶⁾ It is worth noting that if we move the position of the cross-section plane from the image plane to the position Z_{im} , we would obtain $\eta \simeq 0.1$ with spacings equal to $2.9 \mu m$ and $2 \mu m$ respectively for C^- and C_2^- ions instead of $3.1 \mu m$ at position Z_a .

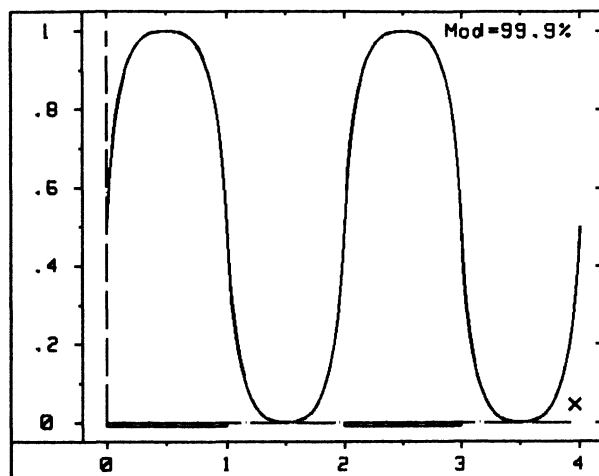


Fig. 8. — Illumination given by the complete objective lens for a test-sample made of parallel bars periodically spaced, the period λ being twice the width b of a bar. The observation plane is the image plane defined by $\Phi_{om} = 0.1$ eV and the limits 0 and 20 eV of the energy passband and the ions being used are C^- . The width of the geometrical image of a bar is $28 \mu\text{m}$ (magnification $K \simeq 8.5$). The illumination is normalized to unity for a uniform sample. The X -axis is orthogonal to the direction bars and is graduated in Kb units.

a spacing two times smaller, $\lambda = 0.5 \mu\text{m}$, would produce an perceptible modulation ($\theta \simeq 0.1$), we reach the conclusion that periodic structures can be resolved fairly beyond of what is suggested by the value of D_{im0} .

However, there is clearly a fundamental difference between “surface imaging” and “analytical imaging”. In the first case, one looks for the finest distinguishable details in the sample and secondary ion emission is used to provide us with a special type of contrast directly related to the chemical composition. In the second case, the aim is to get information upon the chemical or isotopic composition of the sample on the smallest possible scale. In this last case, to characterize the possibilities of the analysis one must define something like a “spatial limit of analytical discrimination” by adding some adequate criteria. For instance, for a test sample with a structure similar to the previous one, in which the substrate would contain one of the elements composing the bars, one might be interested in the smallest spacing λq consistent with the detection of a given concentration in the substrate or with the determination of a concentration ratio with a given precision. Of course, such a definition should be implemented with counting statistics and calibration considerations. This last point reminds us with the fact that if E_{max} deviates too much from E_i , calibration may become a serious problem. Alternatively, if the structure of the sample were known by some other means, one could make assumptions on the composition and try to reconstruct the observed illumination with the help of the spread function $f(r)$. More ambitiously, if counting statistics were high enough, one could hope to reconstruct the structure and composition of the sample.

5. Transmission and spatial resolution.

Table I shows that the objective lens transmission is multiplied by a factor of about 30 when Φ_{om} goes from 0.1 eV to 5 eV. Since at $\Phi_{om} = 5$ eV transmissions are about 85% for C_2^- and 50% for C^- , there is little to gain by increasing Φ_{om} beyond 5 eV for ions like C_2^- and at most a factor

of 2 for C^- ions⁽⁷⁾. Unfortunately, with the increase of Φ_{om} the spatial resolution given directly by the objective lens deteriorates (Tabs. II and III). In those conditions, the use of an ion probe allows to keep the advantage of high transmission while restoring spatial resolution capabilities. Indeed, as long as the probe diameter is larger than the range of the collision cascades triggered off by the impact of a primary ion, the area from which secondary ions escape is about the same as the impact area of the probe. The advantage to be emphasized here, is that the probe size and the objective lens transmission are presently decoupled parameters.

Now if one would wish to reach a lateral resolution in the range of $0.1 \mu\text{m}$ with the objective lens in the direct imaging mode, the beam would have to be stopped down to something like $\Phi_{om} \approx 0.001 \text{ eV}$ and this implies a transmission reduced by a factor of about 100. The comparison between imaging with a probe and direct imaging gives a ratio of 3000 for the transmissions. One may strive for better objective lenses, higher accelerating voltages and a better balance between Φ_{oi} , Φ_{os} and Φ_{om} , the transmission gap seems difficult to fill. However, one must realize that limitations due to the mass spectrometer may slow down this "race" for high transmissions. It is well known that different ionic species with the same number of mass units may be produced in secondary ion emission. Those multiplets can be resolved by a mass spectrometer working at high mass resolving powers, several thousands are often sufficient. Resolving powers in that range can be obtained with some sacrifice in transmission or in field of view size for direct imaging.

6. Spectrometer limitations.

To illustrate this matter, let us first place a small ion probe in the central point and consider the beam stemming from the impact area. For the objective lens working in the accelerating mode, the contrast diaphragm must have a diameter of about $1350 \mu\text{m}$ to set Φ_{om} at 5 eV. Then, if the size of the geometrical probe image is small enough to be neglected, the diameter D_a is equal to about $250 \mu\text{m}$ in the image plane at a distance of 133 mm. from the crossover (Tab. III). The dimensions of the secondary ion beam are of the same order as those given by the objective lens working in the direct imaging mode when Φ_{om} is set to 0.1 eV by a contrast diaphragm of $220 \mu\text{m}$ in diameter at the crossover and the field of view limited to about $220 \mu\text{m}$. Although the two situations are quite different, the envelope of the beams entering the spectrometer are about the same and lead to a mass resolving power of about 400.

One of the most conspicuous difference between the "microprobe" and the "microscope" situations described here above, is that the waist of the beam is located in the image plane in the first case and in the crossover plane in the second case (Fig. 9) so that, from the spectrometer side, the entrance and the aperture diaphragms would be seen in a reverse order. But it could easily be corrected for that inversion with an additional lens. Another difference is that until now only a fixed probe has been considered. Obviously, if the probe is rastered over the sample surface, its aberrated image moves in the image plane. To maintain the beam at rest with respect to the spectrometer while the impact area moves on the sample, one needs to add auxiliary deviating plates at the exit of the objective lens. Those plates are powered in synchronism with the raster of the probe so as to cancel the motion of the secondary ion beam (dynamic transfer). Thus, on the spectrometer side, the beam is seen at rest with the same dimensions and this "trick" increases "artificially" the acceptance of the spectrometer for a given mass resolving power. Of course, from an optical standpoint it would be better to move the sample instead of moving the probe.

Improvements in mass resolving power imply a reduction of the dimensions of the beam seen from the spectrometer side. This can be achieved with additional lenses [17, 18]. Without going

⁽⁷⁾ One should be cautious about those transmission evaluations because they rest on the assumption of the validity of the cosine law for all energies which is at best a convenient approximation.

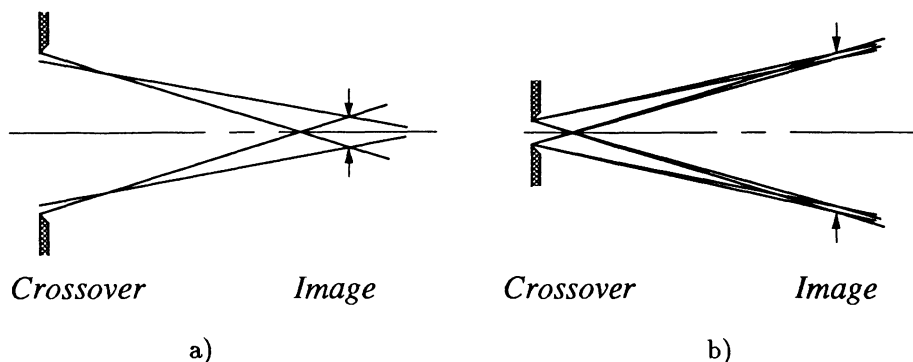


Fig. 9. — Polychromatic beam (0 to 20 eV) in real space for a probe (a) and a direct imaging configuration (b). (a) The beam emitted by the central object point is stopped down to $\Phi_{om} = 5$ eV, the crossover has a diameter $\simeq 1350 \mu\text{m}$, the aberration disk a diameter $\simeq 250 \mu\text{m}$ and are 133 mm apart. (b) The beam emitted from the surface sample is stopped down to $\Phi_{om} = 0.1$ eV, the crossover ($200 \mu\text{m}$) and the aberration disk ($\simeq 30 \mu\text{m}$) but with an aperture diaphragm of $1300 \mu\text{m}$ in diameter at 133 mm would limit an object field of view of $220 \mu\text{m}$.

into details let us give an example and consider the adequate arrangement of lenses which will produce a crossover of about $60 \mu\text{m}$ in diameter in the direct microscope mode. To have comparable beam dimensions in the microprobe situation, we will take a beam stopped down to $\Phi_{om} = 2$ eV and then reduce its crossover to $60 \mu\text{m}$. In the latter case, the initial crossover ($970 \mu\text{m}$) must be divided by about 16 and, because of the optical invariant, this strong reduction produces a strong increase of the image aberration disk diameter ($800 \mu\text{m}$) at the level of the aperture diaphragm of the spectrometer. In the microscope situation, the demagnification of the crossover is much smaller, since the initial crossover for $\Phi_{om} = 0.1$ eV is $200 \mu\text{m}$, but the optical invariant works in the same direction so that an aperture diaphragm of the same diameter as that of the aberration disk in the former case, would now limit a field of view of about $65 \mu\text{m}$. Such an arrangement will produce a mass resolving power of about 1300 and a transmission loss, in the case of microprobe situation, of the order of 2 (Tab. I).

If, in the microprobe situation, one keeps reducing the crossover size, the aberration spot diameter will keep increasing at the level of the aperture diaphragm and this diaphragm will limit transmission. This is typically the kind of limitations one will encounter in trying to get the best transmission at high mass resolution. As for the microscope situation, a further reduction of the crossover will have the effect of reducing the field of view. A compromise can be worked out with a slit being placed on the $60 \mu\text{m}$ crossover. In the example given here, a slit width of about $20 \mu\text{m}$ would give a mass resolving power in the range of 4000 and divide the transmission by about 2.4 (which makes a loss of about 5 when compared to a mass resolving power of 400 in the probe mode). In those last conditions, transmission evaluations give, in the probe situation, 10% and 20% respectively for C^- and C_2^- ions, the ratio of transmissions in the probe and microscope situations being of the order of 15.

The problem of matching the acceptance of the spectrometer with the beam stemming from a small probe impact area is much more involved than the above considerations might suggest. The example here examined has shown that the objective lens aberrations, even in the probe situation, play an important part in controlling the dimensions of the beam entering the spectrometer. However, many important points have been left aside, among others, those concerning aberration corrections of the mass spectrometer and beam shaping with cylindrical lenses to get a better

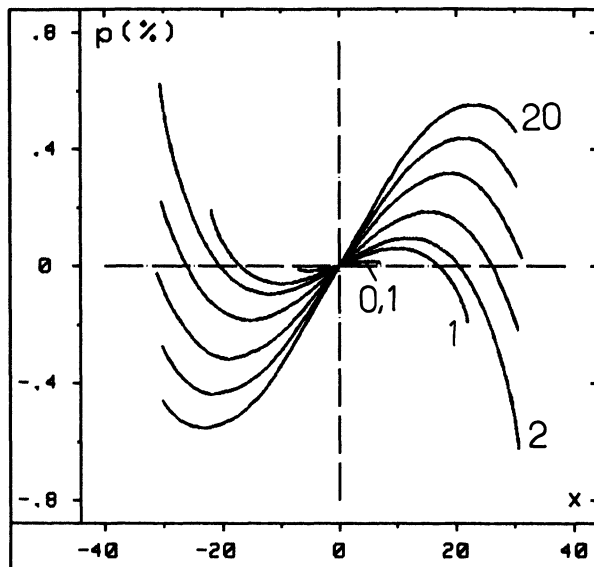


Fig. 10. — Trace diagram of the beam after demagnification of the crossover with an additional lens. The initial conditions are those of figure 3, the crossover shown in figure 3a is demagnified to about $60 \mu\text{m}$.

match. Besides, the numerical methods which have been used here can provide us with means for calculating the intensity mass line profiles and from there it will be possible to determine how to stop down the beam at lower transmission cost for high mass resolution. With an instrument well optimized, one may hope to reach a mass resolving power of 5000 with the transmission previously estimated for $\Phi_{\text{om}} = 5 \text{ eV}$ at a resolving power of 400.

Let us make a last remark concerning the transformation of the beam structure being produced by an additional lens. In figure 10, the trace diagram of the beam stopped down to $\Phi_{\text{om}} = 2 \text{ eV}$ is shown in the crossover plane after reduction to $60 \mu\text{m}$. The shape of this diagram, which is quite different from the diagram shown in figure 3a before reduction, is due to the fact that chromatic aberrations of the objective lens produce a large dispersion, along the optic axis, of the caustic curves belonging to the different energies composing the beam. The additional lens is placed right in the middle of those caustic curves so that many energies may have a trajectory crossing the optic axis at the corresponding first focal point of the lens. These trajectories will emerge parallel to the optic axis ($p = 0$) and their representative point in the trace diagram will lie on the x -axis. The shapes of the Γ curves result from this particular configuration. Another difference with the situation described in the figures 3 is that the waist of the beam does not coincide with the aberrated image of the central point since the crossover and the aberrated image have diameters of $60 \mu\text{m}$ and $800 \mu\text{m}$ respectively. However, it is in the plane of the aberrated image that the separation of aberration spots stemming from neighbouring points of the sample have the best separation as it has been already mentioned in paragraph 2.2.4.

7. Conclusion.

The aberrations of the objective lens have been weighted by the evaluation of the intensity distribution. It has been examined how the illumination of the aberration spot depends upon the upper limit of the transverse energy and upon the shape of the initial energy distribution. An

evaluation has been given of transmission and lateral resolution in rather realistic conditions. It has led us to state the need for a specific parameter, the spatial limit of analytical discrimination, defining the capabilities of an analytical microscope. The probe is certainly the best approach for submicrometer resolution. In this case, the objective lens can be used as an efficient collecting system but its aberrations may limit the transmission when the spectrometer works at high mass resolving powers.

Important questions concerning direct imaging have been left aside such as field aberrations and effects due to the relief on the sample for which there is no more rotational symmetry to simplify the intensity weighting of aberrations. But this study has provided us with solid grounds for future improvements of direct imaging. Those are possible if higher accelerating voltages are used and with a suitable choice of Φ_{om} , Φ_{oi} and Φ_{os} . Moreover a better design of the electrodes should allow to reduce the aberration coefficients of the convergent section of the objective lens which have an important contribution to the deterioration of the image. This later aim should be easier to achieve with normal incidence of the beam [13].

All those efforts to improve the direct microscope may seem out of purpose in circumstances where the probe mode achieves the best lateral resolution at the highest transmission. However, one should not forget, on the one hand, that the search for reduced aberrations also favors transmission in the probe mode and, on the other hand, that it may not be always possible to produce small and intense probes. This last situation may occur with bombardements with low energy particles or when the primary particles have no electrical charge or when the sample is self emitting such as for thermal emission or surface ionization.

References

- [1] MÖLLENSTEDT G. and LENZ F., *Adv. Electron. Electron Phys.* **13** (1963) 259-329.
- [2] CASTAING R. and SLODZIAN G., Proc. Eur. Conf. on Electron Microscopy, Delft, **Vol 1** (1960) pp. 169-72.
- [3] CASTAING R. and SLODZIAN G., *J. Microsc. (Paris)* **1** (1962) 395-410.
- [4] SLODZIAN G., *Ann. Phys. (Masson, Paris)* **9** (1964) 13^{ème} série.
- [5] SLODZIAN G., *Adv. Electron. Electron Phys. suppl.* **13B** A. Septier Ed. (Acad. Press, NY, 1980) pp. 1-44.
- [6] CASTAING R. and SLODZIAN G., *J. Phys. E.: Sci. Instrum.* **14** (1981) 1119-1127.
- [7] LIEBL H., *J. Appl. Phys.* **38** (1967) 5277-5283.
- [8] LIEBL H., *Inst. Phys. Conf. Ser.* **38** (1978) 266-281.
- [9] WAUGH A.R., BAYLY A.R. and ANDERSON K., Proceedings IVth Int. Conf. on SIMS, Osaka, 1983, A. Benninghoven *et al.* Eds. (Springer Verlag, 1984) p. 138.
- [10] LEVI-SETTI R., CROW G. and WANG Y.L., *Scanning Electron Microsc.* **II** (1985) 535-551
- [11] SCHUELER B., SAUNDER P. and REED D.A., Proceedings VIIth Int. Conf. on SIMS, Monterey, 1989, A. Benninghoven *et al.* Eds. (John Wiley, 1990) p. 851.
- [12] SCHWIETERS J., CRAMER H.G., HELLER T., JÜRGENS U., NIEHUIS E., ZEHPFENNING J.F., BENNINGHOVEN A., *J. Vac. Sci. Techn.* **A9** (1991) 2864.
- [13] SLODZIAN G., DAIGNE B., GIRARD F., BOUST F., HILLION F., *C.R. Acad. Sci. Paris* **311** (1990) 57-64.
- [14] LEJEUNE C. and AUBERT J., *Adv. Electronics and Electron Phys. Suppl.* **13A**, A. Septier Ed. (Acad. Press (NY) 1980) pp. 159-259.
- [15] SLODZIAN G., *Scanning Microscopy Supplement* **1** (1987) 1-12.
- [16] BAUER E., *Ultramicroscopy* **17** (1985) 51.
- [17] SLODZIAN G., Natl. Bur. Stand. (US), Spec. Publ. **427** (1975) 33-61.
- [18] SLODZIAN G. and FIGUERAS A., Proc. Int. Conf. X-Rays Opt. Microanal. 8th 1977, (Michigan: Midland Pendell, 1980) pp. 659-665.